

Available online at [www.sciencedirect.com](http://www.sciencedirect.com)

**jmr&t**  
Journal of Materials Research and Technology  
journal homepage: [www.elsevier.com/locate/jmrt](http://www.elsevier.com/locate/jmrt)



# Experimental investigation of polycarbonate sheets deformed by SPIF: formability, micro-mechanisms of failure and temperature analysis

A. Rosa-Sainz <sup>a</sup>, G. Centeno <sup>a,\*</sup>, M.B. Silva <sup>b</sup>, C. Vallellano <sup>a</sup>

<sup>a</sup> Department of Mechanical and Manufacturing Engineering, School of Engineering, University of Seville, 41092, Seville, Spain

<sup>b</sup> IDMEC, Instituto Superior Técnico, Universidade de Lisboa, Av. Rovisco Pais, 1049-001 Lisboa, Portugal

## ARTICLE INFO

### Article history:

Received 9 January 2023

Accepted 9 July 2023

Available online 17 July 2023

### Keywords:

Polycarbonate

Single point incremental forming

Forming limit diagrams

Failure

Scanning electron microscope

Temperature analysis

## ABSTRACT

This article presents an experimental research performed on a polycarbonate sheet deformed by single point incremental forming (SPIF). The analysis is implemented within the framework developed in previous research work for assessing formability and failure by necking and fracture of polymeric sheets in conventional and incremental sheet forming (ISF) processes. The experimental plan is taking into account a series of process parameters, including tool diameter, feed rate, spindle speed and step down. The results allow an evaluation of the influence of these parameters on the formability and their effect on the failure modes. In this regard, three modes of failure were observed: fracture, twisting and crazing. It was shown that most of the typical forming conditions in SPIF lead to failure by fracture in the absence of necking (crack opening in mode I), and all the test conditions presented a combination of twisting and fracture. Higher values of the step down increased the intensity of twisting whereas high values of spindle speed resulted in crazing. A scanning electron microscopy (SEM) evaluation was performed as well as an integral temperature analysis to provide a complete window for understanding the conditions upon which the different failure modes of this thermoplastic material are developed in SPIF.

© 2023 The Authors. Published by Elsevier B.V. This is an open access article under the CC BY-NC-ND license (<http://creativecommons.org/licenses/by-nc-nd/4.0/>).

## 1. Introduction

Polycarbonate (PC) is a polymeric material that was first developed simultaneously by Bayer AG in Germany and by General Electric in the USA in the early 50's of last century [1], and has nowadays become one of the most commonly used amorphous polymers in engineering. PC is a thermoplastic polymer with high transparency, high ductility, impact

resistance and light weight. In addition, insulation as well as other electrical characteristics of PC are excellent, and they remain almost constant with temperature changes and humidity conditions. During the last decades, PC has been widely used in engineering applications, being one of the reasons that it can be formed into any shape with excellent performance. PC is usually supplied in neat and glass fiber reinforced grades and can be processed by all thermoplastic processing methods. The most common processes are

\* Corresponding author.

E-mail address: [gaceba@us.es](mailto:gaceba@us.es) (G. Centeno).

<https://doi.org/10.1016/j.jmrt.2023.07.075>

2238-7854/© 2023 The Authors. Published by Elsevier B.V. This is an open access article under the CC BY-NC-ND license (<http://creativecommons.org/licenses/by-nc-nd/4.0/>).

injection moulding sheet and profile extrusion, being these operations only economically viable for mass production [1].

Currently, the industry trends are more and more aligned with low volume, light weight, high quality and customization of products. To this regard, the scientific term “Industry 4.0” was first introduced in Germany in 2011, used for denoting the notably transformation process in the global chains of value creation, being the main objectives of this Industry 4.0 connecting multiples devices, machines, sensors, and people to conduct process monitoring, adaption, and optimization [2]. These objectives have been recently extended in the novel framework of Industry 5.0 [3].

To this regard, the main aims of today’s industry are in concordance with the deterministic incremental sheet forming (ISF) technologies, and especially with its simplest process variant: single point incremental forming or SPIF, which is a low cost and flexible dieless forming process, especially suitable for the production of small batches or prototypes. In SPIF, a sheet blank is progressively deformed by the action of a spherical-end forming tool guided to follow a pre-established trajectory in a numerical control machine (CNC) in order to produce the final part geometry.

The main advantage of applying ISF to polymer sheets is that the process can be still carried out at room temperature (RT) achieving high levels of material formability. SPIF has been applied for the manufacturing of metallic components for different industrial sectors as the automotive [4], the aerospace [5] as well as the biomedical field [6,7]. However, polymer sheets show different behaviour compared to metal sheets and, to this respect, research works have been focusing on understanding the mechanical behaviour of these polymeric materials deformed by SPIF/ISF.

In this regard, Franzen et al. [8] was pioneer in demonstrating the feasibility of SPIF for producing sheet parts made of polyvinyl chloride (PVC), also pointing out the main two modes of failure in SPIF of polymers, i.e. wrinkling (or twisting) and fracture. Soon after, Martins et al. [9] studied five thermoplastic polymers confirming the potential of SPIF for the manufacturing of customised parts. This work made use of conical testing geometries allowing the identification of the most significant process parameters and material properties. In addition, in the work by Martins et al. [9], three main failure modes for polymers in ISF were identified: (i) crack opening along the circumferential direction, (ii) twisting (or wrinkling), which consists on the development of wrinkles along the sloped wall of the parts, and (iii) crack opening along the bisector direction in the inclined wall of the parts. Within this research line, Silva et al. [10] proposed in 2011 a theoretical model based on membrane stresses for SPIF of polymers under plane strain conditions, being the keynote influential process variables identified for the case of PVC.

More recent works have been focusing on the effects of process parameters in the resulting polymer parts deformed by SPIF. In this sense, Davarpanah et al. [11] studied the mechanical properties and the chain orientation of the formed component by SPIF for both amorphous (PVC) and semi-crystalline (polylactic acid or PLA) polymers. Le et al. [12] studied the formability of thermoplastic sheets in terms of the maximum forming wall angle reached in SPIF without tearing and/or failure. In terms of electric energy consumption and

temperature variations in SPIF of polymers, Bagudanch et al. [13] carried out an investigation concluding that the manufacturing of polymeric parts via SPIF reduces the energy consumption with respect to conventional forming processes. More recently, Durante et al. [14] evaluated the influence of the contact conditions at the tool-work piece interface and the toolpath strategy on the quality of SPIFed PC formed parts. Regarding the influence of the tool path strategy on the modes of failure, Yang and Chen [15] evaluated an alternate spiral tool trajectory in order to reduce the twisting mode of failure, and included a new analytical model to calculate the twist angle for polyether-ether-ketone (PEEK) material.

Very recently, a previous work by the authors [16] presented an experimental investigation of PC truncated cones deformed by SPIF, aiming the evaluation of the influence of the main process parameters in the material formability and the resulting mode of failure. Also in this work, three modes of failure were observed for PC in SPIF: fracture, twisting, and crazing. The failure mode by crazing was identified when the temperature increased due to the increase in the spindle speed in SPIF of polycarbonate sheet, showing microcracks that grew in the specimen as a result of the process cavitation. This study was carried out in terms of principal strains that were evaluated within the material forming limit diagrams (FLDs) obtained independently by means of conventional Nakajima tests making use of digital image correlation (DIC). The adaptation of methodologies commonly applied to metals [17,18] for determining the formability limits by necking was proposed to be used in thermoplastic polymers. Finally, the results indicated that the FFL obtained via a DIC [19] has to be considered as the actual fracture limit due to the significant elastic recovery produced in the PC sheet.

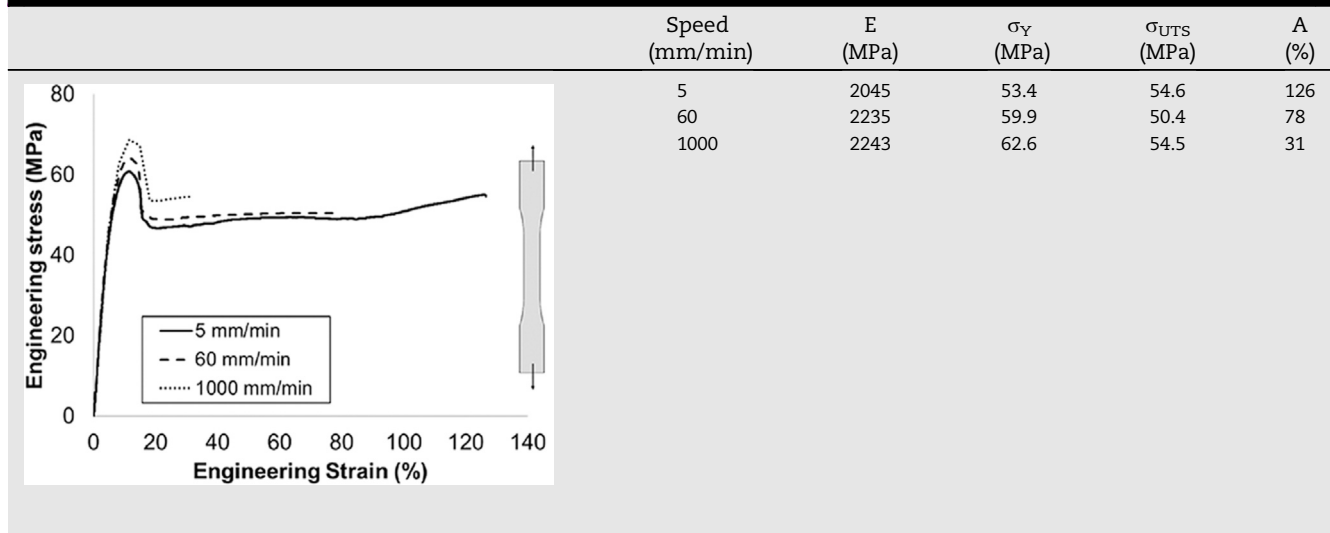
In this context, the present paper proposes an experimental investigation on SPIF of 2 mm thickness PC sheet using a frustum pyramidal geometry that excites strain states from plane strain towards biaxial strain as approaching to the pyramid corners. To this regard, the study analysed the influence of a number of process parameters (tool diameter, feed rate, spindle speed and step down) in formability and the resulting modes of failure. The micro-mechanisms of failure were also analysed in detail by using scanning electron microscopy (SEM) focusing on the distinctive failure patterns of each set of process parameters. Furthermore, a comprehensive temperature analysis was conducted in order to provide a better understanding of the conditions upon which the different modes of failure (i.e. fracture, twisting and/or crazing) are developed in SPIF.

---

## 2. Experimentation

### 2.1. Material characterization

The mechanical characterization of 2 mm thickness PC sheets (Supplied by RS PRO® in blank plates of 1250 mm × 610 mm) was carried out using tensile tests. The tests were performed using an INSTRON 5900 universal testing machine, and were conducted at RT (15–20 °C) in accordance with the ASTM D638-14 standard [20] (using type I specimens). The tensile tests were carried out at a velocity of 60 mm/min, which

**Table 1 – Average true stress-true strain curves obtained and mechanical properties from tensile tests.**

corresponds to the identical speed employed in the Nakajima tests. Furthermore, additional tests were conducted at velocities of 5 mm/min and 1000 mm/min to investigate the material's response under different speeds. In order to ensure repeatability, three repetitions were conducted, and Table 1 presents the average response of the PC material when subjected to a simple uniaxial load at different testing speeds. Table 1 provides the modulus of elasticity (E), the yield strength ( $\sigma_Y$ ), the ultimate tensile strength ( $\sigma_{UTS}$ ), and the elongation at break (A), at 5, 60 and 1000 mm/min.

As anticipated, the Young's modulus and yield stress of PC demonstrate an upward trend with higher velocity values (60 and 1000 mm/min), whereas lower velocity values (5 mm/min) result in a decrease in both the Young's modulus and yield stress, leading to enhanced ductility in the material. This strain-rate and temperature dependent behaviour is commonly observed in thermoplastic materials.

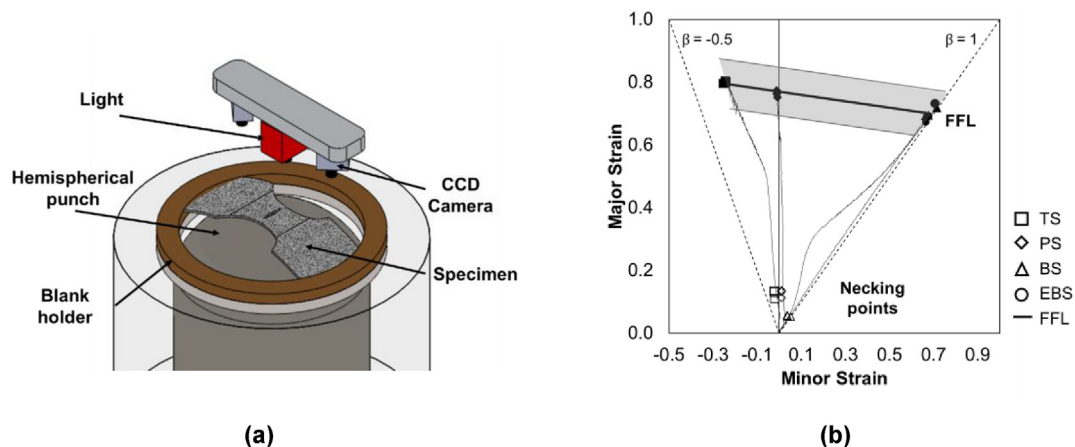
## 2.2. Formability limits by necking and fracture

The material batch of 2 mm thickness PC sheets was provided by an industrial supplier in 1250 × 610 mm laminates and presents 1.2 g/cm<sup>3</sup> of density, 62 MPa of yield stress, 118

Rockwell R hardness and a 70% of elongation at fracture according to the manufacturer data sheet.

The characterization of the material in terms of formability limits by necking and by fracture was performed by means of Nakajima tests. These tests followed the standard ISO 12004–2 [21] and were performed at RT (15–20 °C) using a universal deep drawing machine Erichsen™ model 142–20 with a speed of 60 mm/min. The measurements of the principal strains within the deforming area at the vicinity of the zones where cracks initially appeared were carried out using the digital image correlation system ARAMIS® v6.2.0–6. To this regard, Fig. 1a depicts the schematic representation of the Nakajima test for a plane strain state specimen, in which the PC sheet is being deformed by means of the 100 mm diameter hemispherical punch. The sheet is painted with a black and white stochastic pattern on the specimen's surface to obtain a fine spray of matte black speckles over a white background. The ARAMIS® system is composed of two cameras with a relative angle of 23.6° between them and lens with a focal length of 50 mm.

Different specimen geometries were machined out from the provided sheets and the resulting specimens were aligned in the tests longitudinally with the extrusion direction. These



**Fig. 1 – (a) Schematic representation of the Nakajima test for a plane strain specimen, and (b) formability limits obtained experimentally for the 2 mm thickness PC sheet analysed [16].**

geometries gave place to a number of different loading paths including: Tensile Strain (TS), Plane Strain (PS), Biaxial Strain (BS) and Equibiaxial Strain (EBS), being the specific dimensions of the geometries used and the operating conditions described in the previous paper by the authors [16]. Two layers of polytetrafluoroethylene (PTFE) were sandwiched with three layers of Vaseline between the punch and the polymeric specimen to minimise the friction. In order to provide statistical meaning to the results obtained, three repetitions were made for each Nakajima test specimen geometry.

The formability limit curves (FLCs) of the polymeric sheet associated with necking were determined in the principal strain space by adapting a time-dependent methodology [17] that is commonly applied to metals. This time-dependent methodology is based on the experimental indication of the neck initiation and its progress. The methodology studies the temporal evolution of the major strain and its first-time derivative, i.e. the major strain rate, for a series of points along a section perpendicular to the crack.

On the other hand, the procedure for determining the formability limits by fracture is based on the measurement of thickness at fracture of the failure specimens by using optical microscopy [22]. Minor strain at fracture ( $\epsilon_{2f}^*$ ) and major strain at fracture ( $\epsilon_{1f}^*$ ) were calculated considering that the local loading path slope of the principal strain ratio  $\beta^*$  remains constant, thus being  $\beta^* = d\epsilon_2^{DIC}/d\epsilon_1^{DIC}$  (i.e. considering the last caption provided by the DIC system). In the case of PC, it was noticed that a notably material elastic recovery after fracture is produced. This fact is related to its relatively low value of the Young's modulus of elasticity (around 2.4 GPa). Therefore, in order to define the fracture forming limit line (FFL), the last pair of values of the principal strains provided by the DIC system was considered for defining the principal strains at fracture. Additional information and details concerning the determination of forming limits of the material can be found in previous work by the authors [16,19].

In this sense, Fig. 1b shows the forming limits within principal strain space of the 2 mm thickness PC sheets analysed. The FLC was not plotted in Fig. 1b, but only the

corresponding “necking points”. This is due to the fact that the FLC would not follow a regular shape, such as the typical V-shape of metals or a straight line. As previously explained, The FFL was built by using the values of principal strains evaluated by DIC at the last instant prior to fracture. This allowed the determination of the FFL, which was approximated by Eq. (1) and is represented in Fig. 1b by a straight line with a negative slope of ‘-0.102’ together with a scatter band of the 10%.

$$\epsilon_1^{DIC} = -0.102 \times \epsilon_2^{DIC} + 0.7704 \quad (1)$$

### 2.3. Experimental plan in SPIF

The SPIF experiments were carried out using a spherical-end forming tool driven by a CNC milling machine Emco™ model VMC 100 with Emcotronic TM02 controller, which follows incrementally the pre-established tool path deforming the clamped PC sheet blank into the final truncated pyramid at RT (15-20 °C). In order to minimise friction, lubricant Houghton™ TDN-81 was used between the tool and sheet surface.

A schematic view of the assembly of the SPIF setup is represented in Fig. 2a. The undeformed PC sheet is placed and clamped between the backing plate and blank holder and then the forming tool performs progressively the programmed trajectory allowing the manufacturing of the actual frustum pyramidal testing geometry. All the tests were performed until the instant in which failure occurred. The schematic representation of this frustum pyramid testing geometry including its final dimensions is presented in Fig. 2b. The radius of the top of the pyramid is 20 mm (R1 in Fig. 2b) and the radius of the bottom of the pyramid is defined by the tool radius. The angle  $\varphi$  can be determined by the ratio between  $\varnothing A$  and  $\varnothing B$ , which can be close to 90° in the limit case, i.e. when  $\varnothing A = \varnothing B$ .

In this sense, Table 2 presents the process parameters corresponding to the SPIF experimental work plan. The testing parameters considered were tool diameter ( $\Phi_{tool}$ ), spindle speed (S), feed rate (F) and step down ( $\Delta z$ ). Two replicates were performed in the case that the results

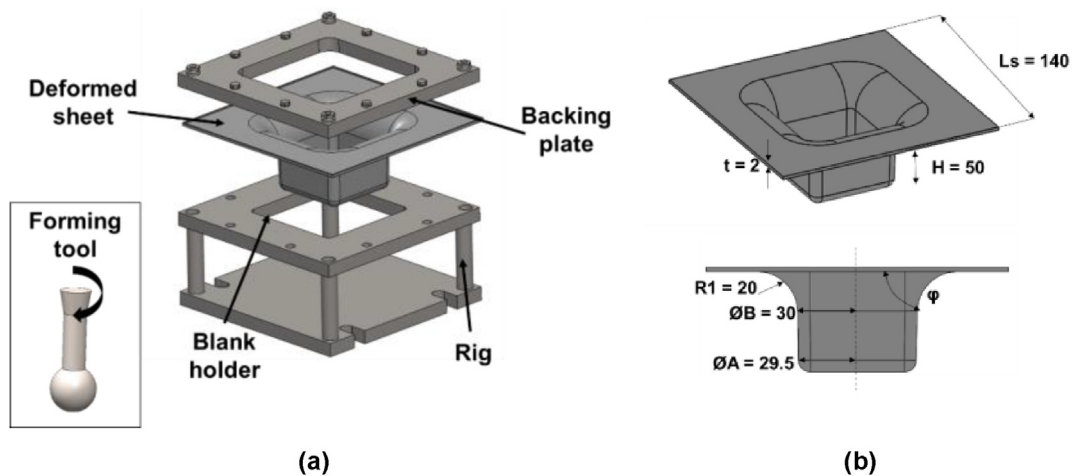


Fig. 2 – Schematic view of (a) the assembly of the SPIF setup and (b) the frustum pyramid testing geometry including its final dimensions.

**Table 2 – SPIF experimental plan for 2 mm thickness PC sheet.**

Test condition (TCx)	Tool diameter (mm)	Spindle speed (rpm)	Feed rate (mm/min)	Step down (mm)
	$\Phi_{\text{tool}}$	S	F	z
TC0	20	20	1000	0.1
TC1	20	20	1000	0.2
TC2	20	20	1000	0.5
TC3	12	20	1000	0.1
TC4	10	20	1000	0.1
TC5	20	500	1000	0.1
TC6	20	1000	1000	0.1
TC7	20	20	500	0.1
TC8	20	20	250	0.1

As was explained before, the SPIF tests were carried out until the instant in which fracture took place, being considered as outputs the final depth and the mode of failure.

showed consistency in terms of the final depth at fracture and the mode of failure attained. In case of discrepancy, 3 or more replicates should be performed, which did not occur during this experimentation.

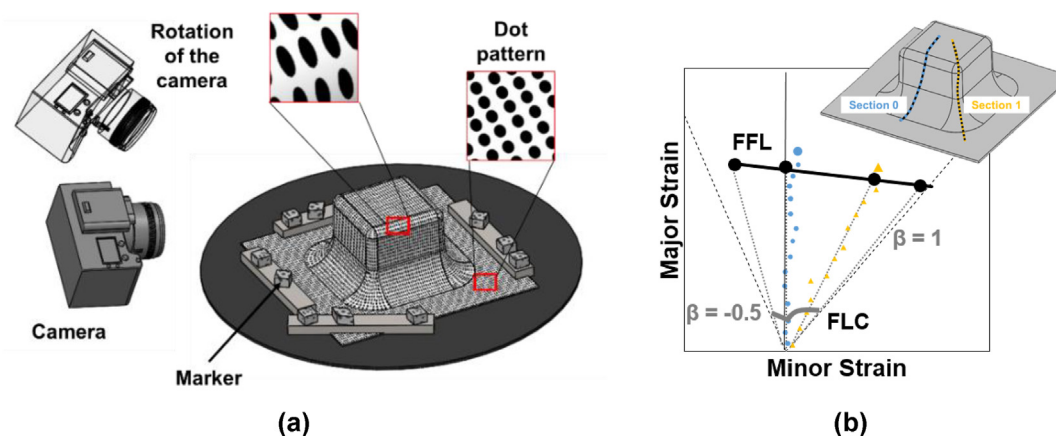
The main aim of this experimental plan was to evaluate and try to isolate the effect of each one of the process parameters considered. For this purpose, a reference test condition named “TC0” was defined with the selected parameters (marked in bold font in Table 2). Other tests were performed (from TC1 to TC8), changing one of the parameters (from the values used in TC0, also in bold) and maintaining the others fixed. Tests were carried out with 10, 12, and 20 mm of tool diameter, 20, 500, and 1000 rpm of spindle speed, 250, 500, and 1000 mm/min of feed rate, and 0.1, 0.2, and 0.5 mm of step down.

### 2.3.1. Strain measurement methodology

The principal strain state was evaluated on the specimens deformed by SPIF using the off-line automated 3D deformation digital measurement system ARGUS® based on circle grid analysis (CGA). The working principle of the ARGUS® system is based on photogrammetry, also called remote sensing. This method allows to compute a three-dimensional geometry on the basis of a set of two-dimensional pictures [23,24]. The

schematic Fig. 3a represents the utilisation of the CGA system ARGUS®, showing the “circular barcode markers” that are needed as a reference by the system. These markers should be placed in the region of the interest and are required for calculating the camera position with respect to the object for each picture. On the other hand, to measure the strains at the surface of the final part, it is necessary that the circle grid is clearly visible on the final specimen. For this reason, a circle pattern of 0.75 mm diameter was carefully printed prior to the tests on the sheet blank surface by means of an ink printing process.

Fig. 3b depicts the procedure sequence for obtaining the contour of the principal strains on the outer surface of the testing geometries. To this regard, Fig. 3b shows two selected longitudinal sections to be analysed by ARGUS® labelled as section 0 and section 1, corresponding to plane strain and biaxial strain conditions, respectively. Fig. 3b depicts a schematic representation of the material FLD obtained independently via Nakajima tests using different strain loading paths, thus providing the conventional forming limits at necking (FLC) and fracture (FFL). Along with this schematic FLC, an illustration of the expected contour of the principal strains along the selected sections attained on the surface of the final testing specimen deformed by SPIF is also



**Fig. 3 – Schematic view of (a) the utilisation of the CGA system ARGUS®, (b) the final SPIFed specimen depicting 2 sections of analysis and the resulting strains within the material FLD.**

**Table 3 – SPIF experimental results for 2 mm thickness PC sheet.**

Test condition (TCx)	Tool diameter (mm)	Spindle Speed (rpm)	Feed rate (mm/min)	Step down (mm)	Twisting visible depth (mm)	Final depth at fracture (mm)	Failure
TC0	20	20	1000	0.1	20.2	25.2	T + F
TC1	20	20	1000	0.2	20.1	28.3	T + F
TC2	20	20	1000	0.5	21.0	30.7	T + F
TC3	12	20	1000	0.1	23.8	24.9	T + F
TC4	10	20	1000	0.1	23.7	24.8	T + F
TC5	20	500	1000	0.1	20.1	25.5	T + F
TC6	20	1000	1000	0.1	20.1	24.8	T + F + C
TC7	20	20	500	0.1	21.7	25.0	T + F
TC8	20	20	250	0.1	21.2	26.5	T + F

provided. As can be seen in Fig. 3b, pyramidal testing geometries produce strain states close to plane strain on the pyramid wall (blue points in Fig. 3b) and also biaxial strain conditions close to the pyramid edges (orange points in Fig. 3b).

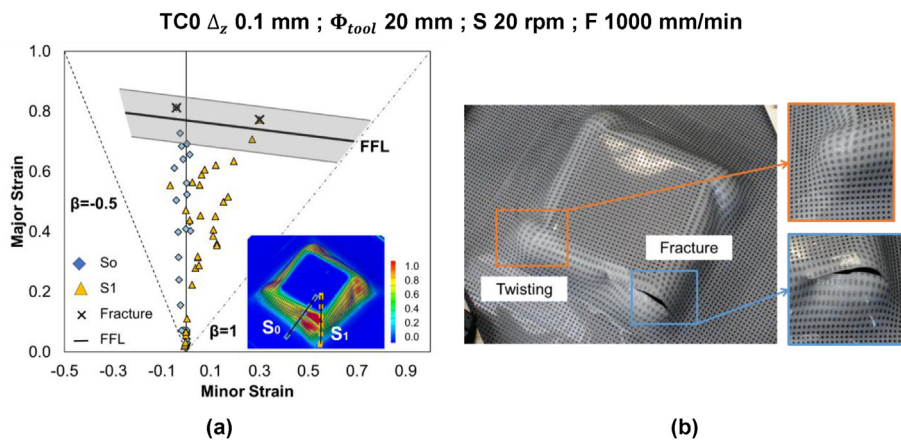
### 3. Results and discussion

Section 3.1 presents the results obtained from the experimental plan performed in SPIF. These results were analysed within the material FLD (Forming Limit Diagram). As explained above, the target process parameters considered were the tool diameter, the spindle speed, the step down and the feed rate. In addition, the resulting modes of failure are presented, discussing the influence of the parameters on these failure modes attained in SPIF of the pyramidal PC testing sheet considered. After that, section 3.2 provides an evaluation of these failures based on the SEM analysis of the microscopic patterns in order to enlarge the understanding of the micro-mechanisms controlling failure. Finally, section 3.3 presents a temperature analysis with the aim of providing a process window for understanding the temperature conditions upon which the different modes of failure are developed in the SPIF experiments.

#### 3.1. Formability and failure in SPIF

Table 3 presents the results obtained for the nine different SPIF test conditions considered in the experimental plan. As can be seen, the PC sheet exhibited three differentiated modes of failure, i.e. fracture, twisting and crazing, as a consequence of varying the process parameters. In fact, these results showed that, for all parameter sets considered, twisting occurred first and then fracture, i.e. at a certain level of tool depth depending on the test, twisting was visually assessed in the pyramid frustum defining the so-called “twisting visible depth”, whereas the “final depth” corresponds to the onset of fracture. In this sense, Table 3 summarises the results providing the corresponding tool depths at the onset of twisting and fracture of each of the testing replicates as well as the corresponding modes of failure attained in each case: fracture (“F”), twisting (“T”) and in one of the cases also crazing (“C”).

Concerning the final depth attained, it must be noticed that formability in SPIF of polymers is not directly related to this final depth at fracture, which can be indicative but not a definitive output parameter. Final depth can be just considered as a qualitative measurement of formability for the different tests performed. Thus, this analysis must be definitively performed in terms of principal strains.



**Fig. 4 – SPIF reference test condition (TC0): (a) FLD along with the contour of major principal strain and (b) the final tested specimen.**

In order to establish a general framework for assessing formability and the mode of failure attained for each set of the process parameters considered, Fig. 4a depicts the Forming Limit Diagrams (FLD's) for the case of the test of reference TC0 (see the set of parameter corresponding to the test in Table 3).

As explained schematically above, the pyramidal frustum geometry considered allowed analysing within the FLD's sections at 2 differentiated zones corresponding both to the principal strains states until fracture in (i) plane strain conditions (labelled as "S0" in Fig. 4a) on the flat lateral surfaces and (ii) biaxial strain states (labelled as "S1" in Fig. 4a) in the region close to the pyramid edges. In addition, along with the FLD's, the contour of the major principal strain provided by ARGUS® onto the final tested pyramid specimen is also represented in Fig. 4a. The FFL's (black lines in the FLD's) determined by means of the Nakajima tests explained in section 2.1 are represented together with a scatter band corresponding to an interval of  $\pm 10\%$  due to the experimental uncertainty. On the other hand, Fig. 4b depicts the final testing specimen, highlighting the zones where twisting and fracture occurred for the case of the test of reference TC0.

Analogously to the case of the test TC0, Fig. 5 shows the resulting FLD's of the rest of the specimens tested, i.e. from test TC1 (see Fig. 5a) to test TC8 (see Fig. 5h). Below is an analysis and discussion of the results obtained from the SPIF tests both in terms of conformability and distribution of observed strains.

To this regard, Fig. 5a and b presents the results corresponding to the variation of the step down concerning test conditions TC1 (0.2 mm) and TC2 (0.5 mm), respectively, presenting both tests twisting combined with later fracture. In the case of TC1, the principal strains corresponding to S0 and S1 are in conditions of nearly plane strain and biaxial strain, respectively, showing the effect of twisting in this principal strain distribution. As can be seen in Fig. 5a for TC1, the strain distribution corresponding to plane strain (S0), has tension and compression states in the pyramid wall zone, deviating the principal strains along S0 to negative values of the principal strain ratio ( $\beta$ ) due to the appearance of twisting. In the same sense, section S1, located by the pyramid corner, showed a change in the strain distribution along the section from plane strain to biaxial strain states, i.e. the strains along S1 show a deviation towards higher positive values of  $\beta$  prior to reaching fracture. In this regard, Fig. 5b shows a more noticeable effect on twisting in the strain distribution along the sections due to the increase of step down of TC2 (0.5 mm) compared to TC1 (0.2 mm) and TC0 (0.1 mm). This result can be also observed in the principal strains distributions along sections S0 and S1 depicted in Fig. 5b (test TC2). On the one hand, the minor strain along section S0 has significant negative values corresponding to the tension-compression states exited by twisting at the pyramid wall. On the other hand, the strain evolution along S1 presents a clear non-linear progression because of the effect of twisting by the pyramid wall. In conclusion, it can be pointed out that the step down has a notable effect in the appearance and in the level of the twisting effect, and this level of twisting reached prior to fracture is also rather more visually accused for higher values of the step down.

In addition to that, in terms of formability the strain distributions along the selected sections for TC1 and TC2 analysed using ARGUS® also showed that an increase in the step down produces a slightly increase in the sheet SPIFability. Indeed, as a result of the increase of the step down from TC0 towards TC1 and TC2, an increase of the achievable wall angle, and in consequence an increase in formability is produced. This result is consistent with Davarpanah et al. [9], who studied how the step down in SPIF affects formability in the case of thermoplastic polymers (PLA and PVC). In that work, it was concluded that a greater step down results in an enhancement of spifability up to a certain limit, as far as an excessive step down may lead to premature failure due to the occurrence of twisting. In the same sense, in a previous work by the authors [16] including SPIF tests of PC truncated conical geometries, the results also showed this effect, with twisting occurring for step downs of 0.2 and 0.5 mm, but not for 0.1 mm.

Fig. 5c and d shows the results corresponding to a variation of the tool diameter for the tests TC3 (12 mm of diameter) and TC4 (10 mm), presenting both tests twisting combined with fracture. Nevertheless, the macroscopic analysis of these specimens showed that the twisting effect was not as intense as for tests TC1 and TC2. In TC3, sections S0 and S1 were analysed, again corresponding with the pyramid wall zone and pyramid corner, respectively. In this regards, Fig. 5c showed that the minor strain along S0 presented values close to zero, i.e. corresponding with nearly plane strain. Concerning S1 corresponding to TC3, a slight variation in the strain distribution along the section is attained, deviating the strain state from biaxial to plane strain for high values of the major strain due again to the twisting effect. Concerning the test TC4 (10 mm), the section S0 (wall zone of the pyramid) presents a linear strain distribution within plane strain, whereas along S1 (corner) the strain state evolves in biaxial conditions showing a slight deviation for medium values of the major strain due to a minor twisting. Consequently, it can be concluded that the decrease in tool diameter, which produce a smaller contact area between the tool and the sheet, resulted in a lower twisting effect. This experimental result was more noticeable for TC4 in the sections (S0 and S1) represented in the principal strain space (Fig. 4d), where no negative values corresponding to tension-compression states are attained for S0, and a more linear evolution of the principal strain distribution along S1 (biaxial condition) can be observed. In addition to that, the analysis of TC3 and TC4 using ARGUS® also showed that the decrease in the tool diameter produced an increase in spifability. In this sense, the use of smaller tool diameters concentrates the deformation in a smaller zone, inducing a certain bending effect in the contact zone between the sheet and the tool. This result is consistent with previous works by Martins et al. [9] and Marques et al. [25], in which it was found that the formability of thermoplastics in SPIF is decreased with the increase of tool radius. Nevertheless, it must be also pointed out that other investigations showed the opposite effect, decreasing the material formability in SPIF for smaller tool radii. This is the case of previous research studies by Formisano et al. [26] and Durante et al. [14], in which the formability of PC sheet was slightly enhanced with an

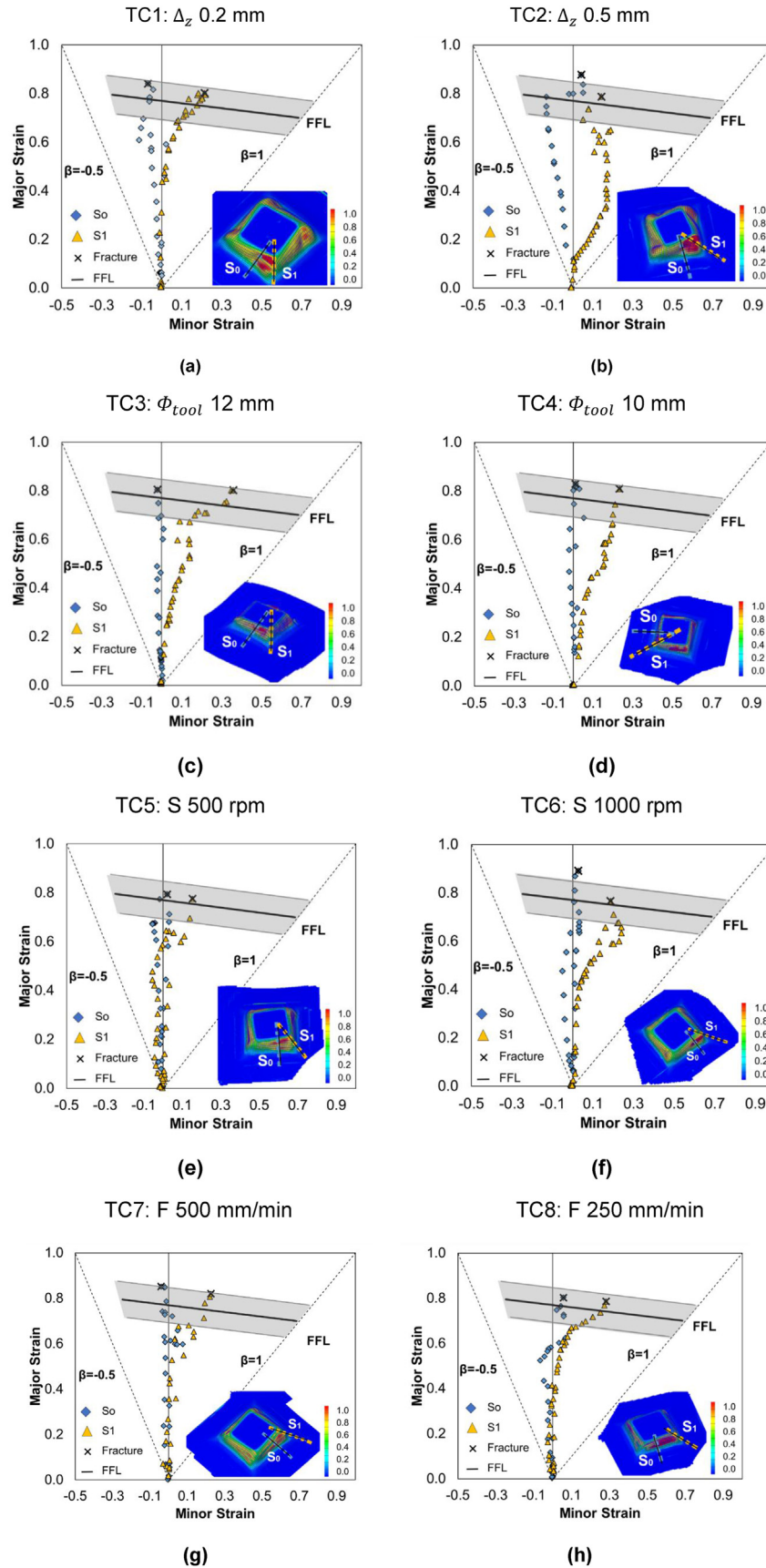


Fig. 5 – FLD's along with the contour of major principal strain on the final tested specimen for each of the SPIF testing conditions considered: from (a) TC1 to (h) TC8.



increase of the tool radius in SPIF forming tests of a varying wall performed with cone and pyramid frustum geometries.

On the other hand, Fig. 5e and f depict the results in terms of principal strains corresponding to a variation of the spindle speed: TC5 (500 rpm) and TC6 (1000 rpm). In terms of the modes of failure attained, TC5 presented twisting and fracture and TC6 showed twisting, fracture and crazing. As can be seen in Fig. 5e, the minor strain along the pyramid wall S0 presents slightly negative values matching the tension-compression states occurred by the effect of twisting. The analysis of the strain distribution along S1 (by the pyramid corner) presents states close to plane strain with very slight deviations towards biaxial strain at high values of the major strain (about 0.6) due to the low effect of twisting by the pyramid wall. As mentioned above, test TC6 (1000 rpm) attained an additional mode of failure beyond fracture and twisting: crazing. As depicted in Fig. 5f, the minor strain along S0 present again negative values as a consequence of twisting, whereas along S1 the strains show a clear trend towards positive values of  $\beta$  for values of the major strain above 0.4 approximately. In addition, the experimental results of TC5 and TC6 indicated that an increase in the spindle speed produced an increase in formability in SPIF. It must be also pointed out that during these two experiments a significant increase of temperature was observed in the specimens, as will be discussed in section 3.3. This fact was also observed in previous work by Bagudanch et al. [27,28], demonstrating that higher values of spindle speed increase formability as a result of increasing the forming temperature. In agreement to that, TC6 (spindle speed of 1000 rpm) achieved a higher level of formability than TC5 (500 rpm). Nevertheless, TC6 was affected by the appearance of the effect of crazing. In this sense, Conte et al. [29] studied the effects of the process temperature of PMMA sheet in SPIF and, according to this work, the appropriate values of the spindle speed should be set in order to not achieve brittle fracture and excessive springback during the process. In sections 3.2 and 3.4 a more detailed discussion of

failure by crazing will be carried out. Moreover, in a previous work by the authors [16], in which SPIF tests were performed using PC sheet and truncated conical geometries, the results also showed the appearance of crazing for a value of 1000 rpm of the spindle speed.

Finally, Fig. 5g and h presents the results obtained by modifying the feed rate with respect to TC0, being the feed rate 500 mm/min for TC7 and 250 mm/min for TC8, respectively, and presenting both tests twisting and fracture. The analysis of the principal strains distributions for TC7 along sections S0 and S1 is represented in Fig. 5g. The minor strain along section S0 was close to zero corresponding to close to plane strain conditions at the pyramid wall, whereas S1 presents a non-linear progression by the pyramid wall from plane strain to biaxial conditions. In the case of TC8, Fig. 5h depicts similar strains distributions of sections S0 and S1 than previous cases. To this regard, the minor strain along section S0 presents negative values whereas the strain distribution along S1 evolves from plane strain to biaxial strain states, as because result of twisting. The comparison between the results obtained for TC7 (500 mm/min of feed rate) and TC8 (250 mm/min) allow concluding that an increase in the feed rate results in an increase of the formability in SPIF. In this sense, some researchers have studied the combined effects of different parameters on formability, as is the case of Le et al. [12] who proved that a combined increase of the step down and the feed rate resulted in a decrease of formability for polypropylene (PP) sheet. To the same regard, the study by Hussain et al. [30] concluded that the formability of PVC sheets increased with the rising ratio between spindle speed and feed rate.

To sum up this analysis of the material formability in SPIF for the 2 mm thickness PC sheet considered, Fig. 6 presents a comparison between the reference test (TC0) and the tests with more different values of process parameters, i.e. with TC2, TC4, TC6, and TC8. In this sense, Fig. 6a presents the results in terms of principal strains corresponding to sections

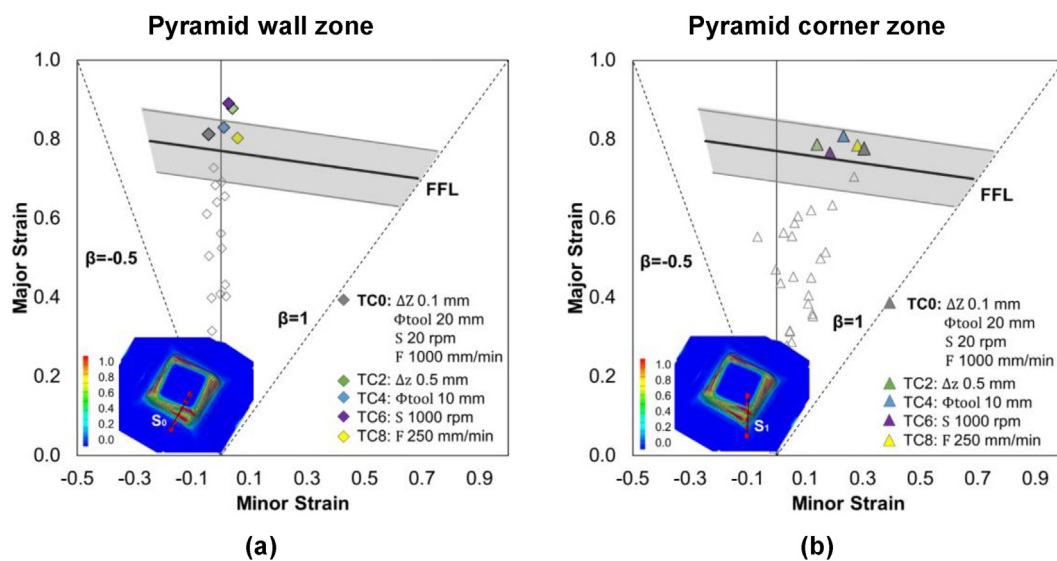


Fig. 6 – FLD for TC0 along with the maximum principal strains at fracture for tests TC2, TC4, TC6, and TC8 in (a) plane strain condition (S0) and (b) biaxial condition (S1).

S0 (by the pyramid wall zone) and Fig. 6b the results corresponding to sections S1 (by the pyramid corner). These Figures depict the strain distribution along the corresponding sections by means of the fracture points for the tests described above (filled dots in Fig. 6a and b), being the strains along S0 and S1 for test TC0 represented in grey colour. It can be seen in Fig. 6a that the two tests achieving the maximum level of major principal strain at fracture were TC2 (increasing the step down from the 0.1 mm of TC0 to 0.5 mm) and TC6 (increasing the spindle speed from the 20 rpm of TC0 to 1000 rpm). Thus, these results revealed that the most relevant parameters in terms of formability were the step down and the spindle speed. On the other hand, the two tests that achieved a minimum level of strain were TC0 and TC8 (feed rate 250 mm/min). In addition to that, it must be also pointed out that except TC2 and TC6, all the fracture strains were within the  $\pm 10\%$  scatter band of the FFL, not varying too significantly the levels of fracture strains attained.

In the case of Fig. 6b, the results for the sections S1 of the different tests analysed at the pyramid corner are depicted. In that case, the maximum levels of major strain at fracture were for TC4 (decreasing the tool diameter from the 20 mm of TC0 to 10 mm) but with very small difference with respect to the other tests. Indeed, all the tests showed a non-remarkable difference in terms of the maximum strains at fracture achieved for the case of biaxial strain state conditions.

In addition to that, a critical comparison in terms of formability and failure with the previous investigation by the authors [16], focusing on SPIF tests with conical geometry with the same material (PC sheets of 2 mm of thickness), must be carried out. On one hand, the experimental results of the previous work led to a number of main conclusions: (i) the increase in the step down favoured the appearance of twisting, (ii) higher values of spindle speeds induced the effect of crazing and, (iii) small tool diameters produced an increase

in formability within in-plane strain conditions for the conical geometry. On the other hand, the pyramidal frustum geometry considered in the present work promoted an intense twisting on the specimen, especially when it was subjected to an increase of the step down. As well as it occurred for the conical geometry, the pyramidal geometry suffered from the effect of crazing due to a higher value of spindle speed resulting in an increase of temperature and the consequent material damage, resulting in this kind of brittle fracture for polymers. To this regard, a new analysis of the micro-mechanism of failure is assessed for the pyramidal testing geometry in section 3.2. Regarding the formability attained, the pyramidal geometry revealed that the step down and spindle speed were the most relevant parameters, whereas for the conical geometry the tool diameter was the key parameters producing the highest levels of formability when small tool diameters were used. This experimental result pointed out the importance of the geometry selected for carrying out a formability analysis in SPIF of polymers.

### 3.2. Micro-mechanism of failure

The examination of the failure surfaces was performed using the JEOL™ model 7001F Scanning Electron Microscope (SEM) with a resolution of 1.2–3.0 nm and a magnification of  $\times 10$  to  $\times 1,000,000$ . In addition, the chemical composition was extracted using Energy Dispersion X-ray Spectroscopy (EDS). Their closer inspection reveals the formation of many voids within the material structure and the phenomenological analysis consisted of a study of the failure surfaces for tests TC0, TC2, TC4, TC6 and TC8 at different magnifications. Furthermore, in the analysis of each case, the chemical composition is presented, including the percentage of carbon and oxygen as elements of the polycarbonate structure and the percentage of chloride due to the lubricant used.

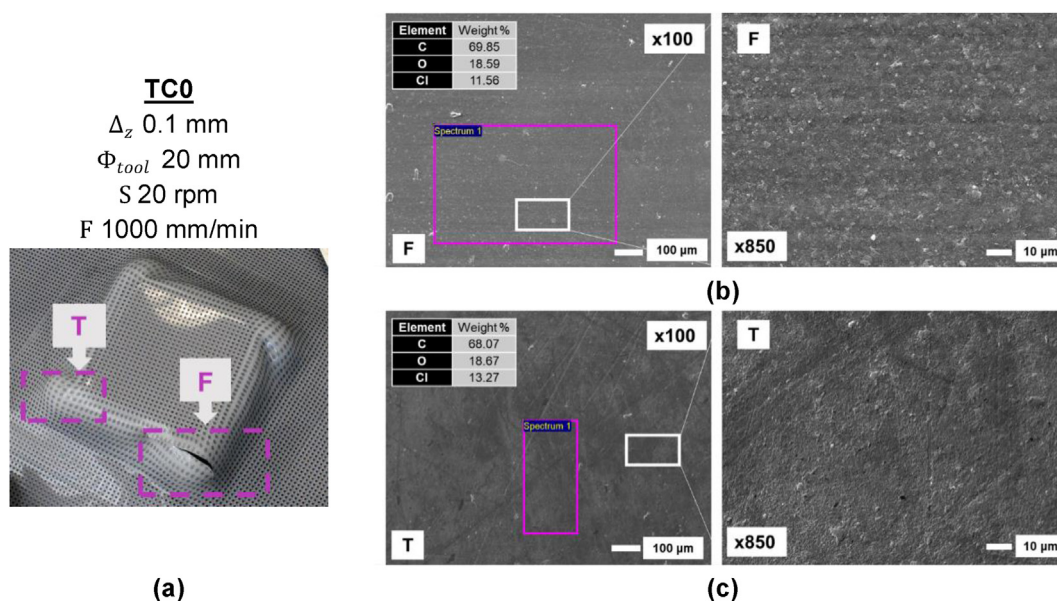


Fig. 7 – TC0 mechanism of failure showing: (a) final specimen, and the failure SEM analysis with  $\times 100$  and  $\times 850$  magnification along with EDS of (b) fracture and (c) twisting surfaces.

PC is an amorphous polymer made up of chains that are disposed in many directions, both entangle and untangle. These strings are able to move and rearrange themselves when tension is applied. In this sense, the flexibility of the links in the chains determines the ease of the chains to slide over each other during deformation [31]. In this regard, the flexibility of polymer chains is related to the mechanical behaviour, and in the case of thermoplastic polymers there are two possible modes of failure: ductile failure (shear yield) and brittle failure (crazing) [32]. The ductile behaviour can be observed in tensile test [19], producing an increase in force with extension, and after reaching the yield point, necking may appear. Continuing the drawing process, the neck extends up to the full length of the specimen, and in case stretching continues, the process might reach the onset of (ductile) fracture. On the other hand, brittle fracture gives place to a dramatic failure that is also called crazing. To this regard, crazes are localised zones of plastic flow, and their closer inspection reveals the formation of many voids within the material structure corresponding to micro-deformation zones. Shear yielding and crazing are not alternative processes that exclude each other. Both can be observed, or only one of them, or even one may follow the other depending on several forming conditions [32].

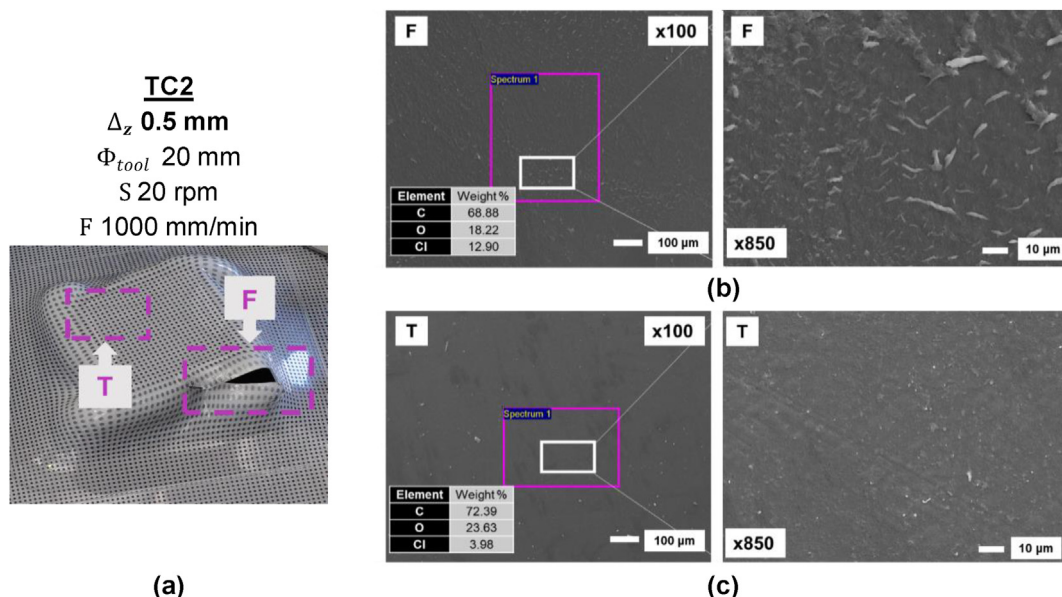
As was explained in section 3.1, in terms of the modes of failure attained, all the SPIF tests presented twisting and fracture, and in the case of the test TC6 (with an increase of spindle speed), the resulting failure mode was twisting, fracture and crazing. The SEM analysis was divided into a number of images (Figs. 7–11) in order to visually depict the fracture (“F”), twisting (“T”) and crazing (“C”) surfaces.

Beginning with test TC0, Fig. 7 depicts the corresponding SEM results obtained. As previously presented, this reference test conditions were step down of 0.1 mm, tool diameter of 20 mm, spindle speed of 20 rpm, and feed rate of 1000 mm/min. Fig. 7a shows the final specimen, indicating the modes of

failure highlighted by means of pink squares at the SEM images. For the case of the fracture surface (“F” in Fig. 7b), the SEM  $\times 100$  magnification exhibited surfaces made up of smooth and rough oval fibers, whereas the  $\times 850$  magnification of the fracture showed spherical shapes on the fracture surface. Zimmerman et al. [33] attributed this quantity of particles to entropy. In that sense, the polymer chains under stress could break away from one another and form strings or long microfibrils, and in consequence, they form spheres in order to have the lowest possible energy under stress. For the case of twisting (“T” in Fig. 7c), the  $\times 100$  magnification showed a smooth surface made up of arbitrary lines, whereas the  $\times 850$  magnification showed areas with more relief than others, resulting in an irregular surface.

In the case of the test TC2 (increased step from 0.1 mm of TC0 to 0.5 mm), it resulted in a combined fracture with more pronounced twisting. To this regard, Fig. 8a depicts the final test specimen, in which the greatest intensity of twisting can be observed. The two failure modes are once again presented, highlighted for each case by means of pink squares in the SEM analysis. In this sense, Fig. 8b shows the SEM results obtained from the selected surfaces as follows: the  $\times 100$  magnification of the fracture surface (on the sheet surface) (“F” in left Fig. 8b) and the  $\times 850$  of a central zone of the fracture area (“F” in right Fig. 8b). In both SEM images, the fracture zone for TC2 showed a homogenous surface formed by stretched fibril structures, different from the previous spheres in TC0. A similar SEM image was observed for polycarbonate material in the work by Jansen et al. [34], in which the surface of the fracture exhibited an extremely smooth morphology. In the same work, the magnification of the fracture surface indicated the presence of these stretched fibrils or striations, having these striations minimal micro ductility, separated by a smaller band showing a very smooth surface morphology.

Fig. 8c shows SEM results in the case of failure by twisting for a  $\times 100$  magnification (left) and  $\times 850$  (right), respectively.



**Fig. 8 – TC2 mechanism of failure showing: (a) final specimen, and the failure SEM analysis with  $\times 100$  and  $\times 850$  magnification along with EDS of (b) fracture and (c) twisting surfaces.**

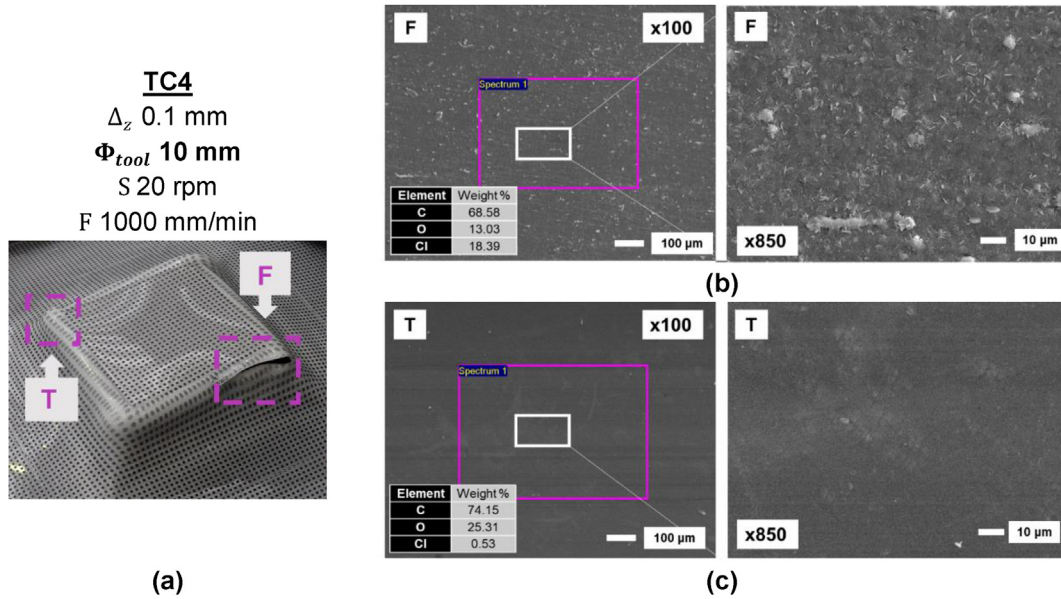


Fig. 9 – TC4 mechanism of failure showing: (a) final specimen, and the failure SEM analysis with  $\times 100$  and  $\times 850$  magnification along with EDS of (b) fracture and (c) twisting.

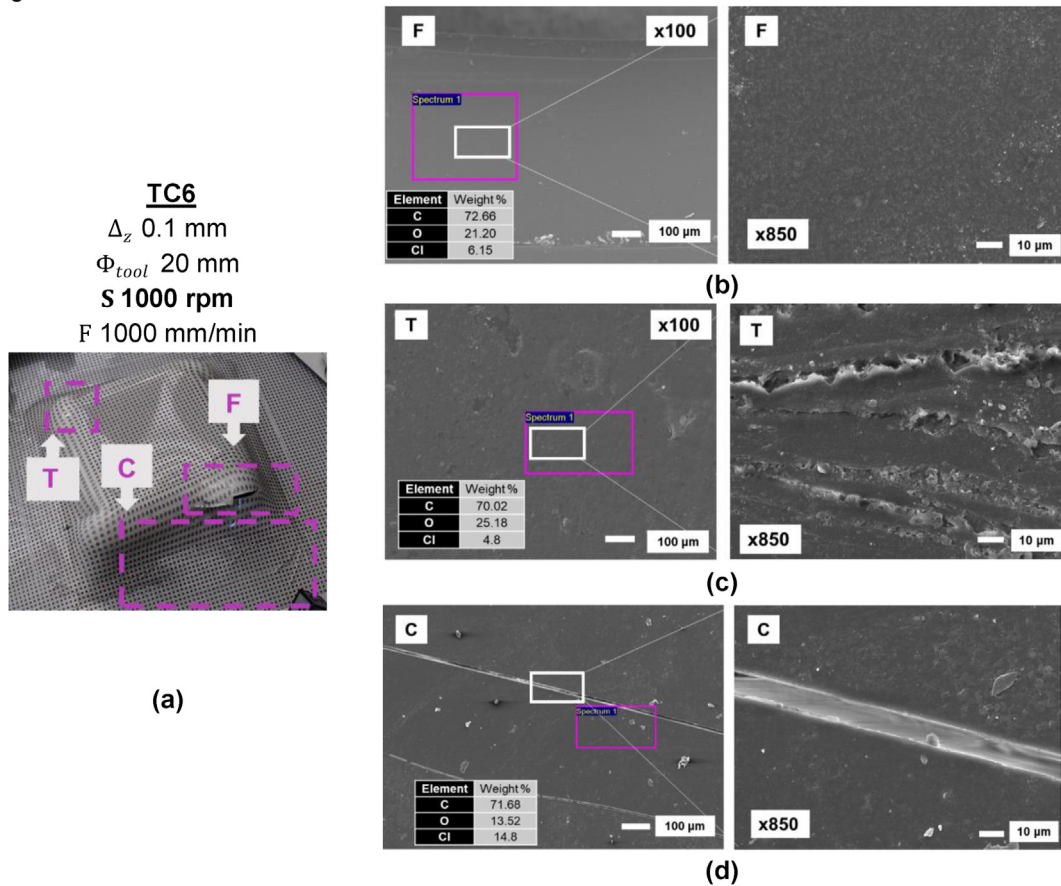


Fig. 10 – TC6 mechanism of failure showing: (a) final specimen, and the failure SEM analysis with  $\times 100$  and  $\times 850$  magnification along with EDS of (b) fracture, (c) twisting, and (d) crazing.

The  $\times 100$  magnification showed a quite uniform area, similar to the prior fracture image (see Fig. 8b), being this smooth area formed by oval shapes together with irregular structures. A similar area was observed by Zimmerman et al. [33], being in this work several spherical particles observed along with strings on the surface near to the fracture. A possible explanation for both surfaces being so similar (fracture and twisting) could be that, since the twisting sample was chosen at the corners of the specimen, this area of twisting was at similar stress levels as that of fracture.

Fig. 9 presents the results for the test TC4, which was obtained by decreasing the tool diameter from 20 mm (TC0) to 10 mm. Macroscopically, Fig. 9a shows a significant reduction in twisting, which may be a consequence of a smaller radius tool that has a smaller area of contact with the sheet resulting in lower friction. As a consequence of this, the twisting effect on the frustum pyramid may be sensibly reduced. On the one hand, Fig. 9b shows that the fracture surface provided by the SEM (“F”) is formed by many spherical fibrils, and the  $\times 850$  magnification also showed elongated granular shapes along with spherical shapes. Furthermore, the twisting surface (“T” in Fig. 9c) with  $\times 100$  (left Fig. 9c) and  $\times 850$  (right Fig. 9c) magnifications showed a uniform and smooth surface as a consequence of the lower intensity of twisting. A similar surface was observed by Wei et al. [35], consisting this study in subjecting polyethylene sheets to ISF tests by varying the plastic strain from 6% to 108%. As expected, this work showed that the density and size of voids increased as the plastic strain increased.

Subsequently, Fig. 10 presents the results of TC6, carried out by increasing the spindle speed from 20 rpm (TC0) to 1000 rpm. As can be seen in Fig. 10a indicated by pink squares, the final specimen exhibited fracture, twisting, and further crazing. On one hand, the SEM analysis of fracture (“F” in Fig. 10b) showed differences with respect to the other tests analysed: the  $\times 100$  magnification depicted a smooth surface

and lines at the top and bottom of the image, whereas the  $\times 850$  magnification of the fracture surface permitted the observation of the wear of the material promoted by its degradation. A similar surface was indicated in the work by Jansen et al. [34], observing smaller concentric rings with very smooth surface morphologies.

On the other hand, Fig. 10b presents the SEM analysis of twisting in TC6, in which the  $\times 100$  magnification (“T” in Fig. 10a) showed a mostly uniform area with several notches, whereas the  $\times 850$  magnification of the twisting surface depicts white threads that craze. As previously discussed, crazes are small cracks that constitute expanded material containing oriented fibrils with voids. In this sense, Fig. 10d shows the SEM image of crazing depicting the fringes along the surface produced by the cavitation process. These brittle fractures are initiated by the formation and growth of voids [32]. In the work by Wei et al. [35] crazing was observed at higher strain levels, noticing the nucleation of micro voids. In this sense, in the work by Jansen et al. [34] the crazing surface indicated the presence of stretched flaps and cycles of craze formation, cracking, and arrest, being these typical characteristics of rapid and unstable crack growth.

Finally, Fig. 11 presents the results of test TC8, obtained by decreasing the feed rate from 1000 rpm (TC0) to 250 mm/min. Fig. 11a indicates the two modes of failure presented in TC8, i.e. twisting and fracture. As can be macroscopically seen in Fig. 11a, the specimen clearly presents a mild twisting. This fact might be related to the duration of the test and the temperature results that will be discussed in section 3.3. Fig. 11b shows the  $\times 100$  (left) and  $\times 850$  (right) SEM magnifications of the fracture surface (“F”). The fracture surface of TC8 exhibited a uniform morphology formed by irregular structures, and also, it was similar to the TC4 (see Fig. 9b). On the other hand,  $\times 850$  magnification showed an area with degradation of the material similar to the prior case of TC6 depicted in Fig. 10b. As

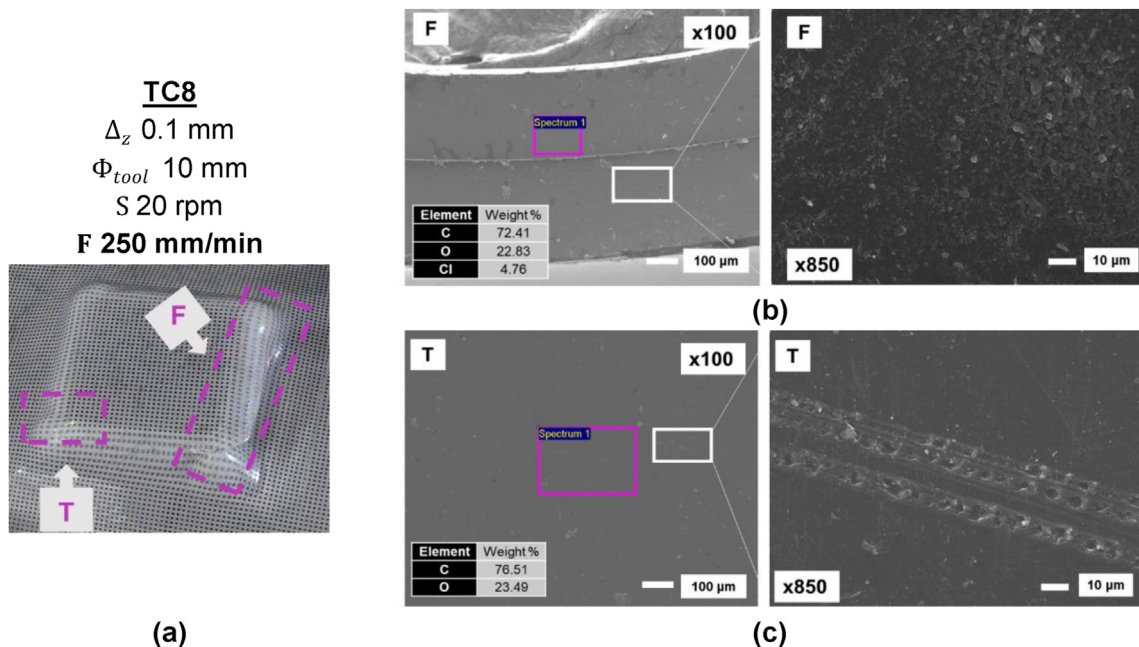


Fig. 11 – TC8 mechanism of failure showing: (a) final specimen, and the failure SEM analysis with a magnification of  $\times 100$  and  $\times 850$  along with EDS of (b) fracture and (c) twisting.


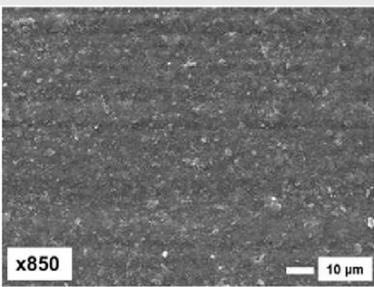

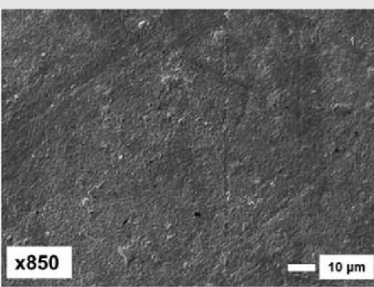
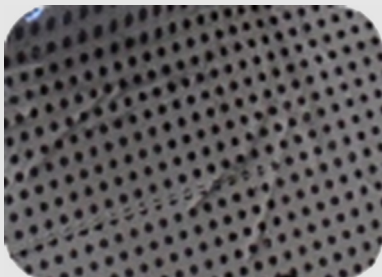
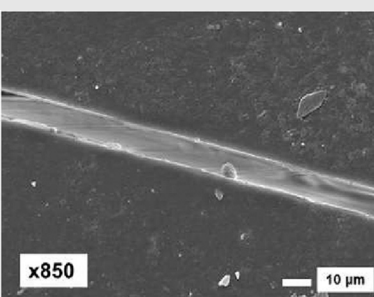
mentioned, this fact may be related to the total duration of the test, as a result of the effect of the prolonged contact with the lubrication. The twist visible at TC8 was more moderate, consistent with the  $\times 100$  magnification presented in Fig. 11c showing a smoother surface. In addition, the  $\times 850$  SEM magnification depicted in Fig. 11c illustrates the presence of holes in the surface. This fact may be related to the environmental stress cracking (ESC) due to the lubricant effect, and is aimed to be studied in more detail in future research by the authors.

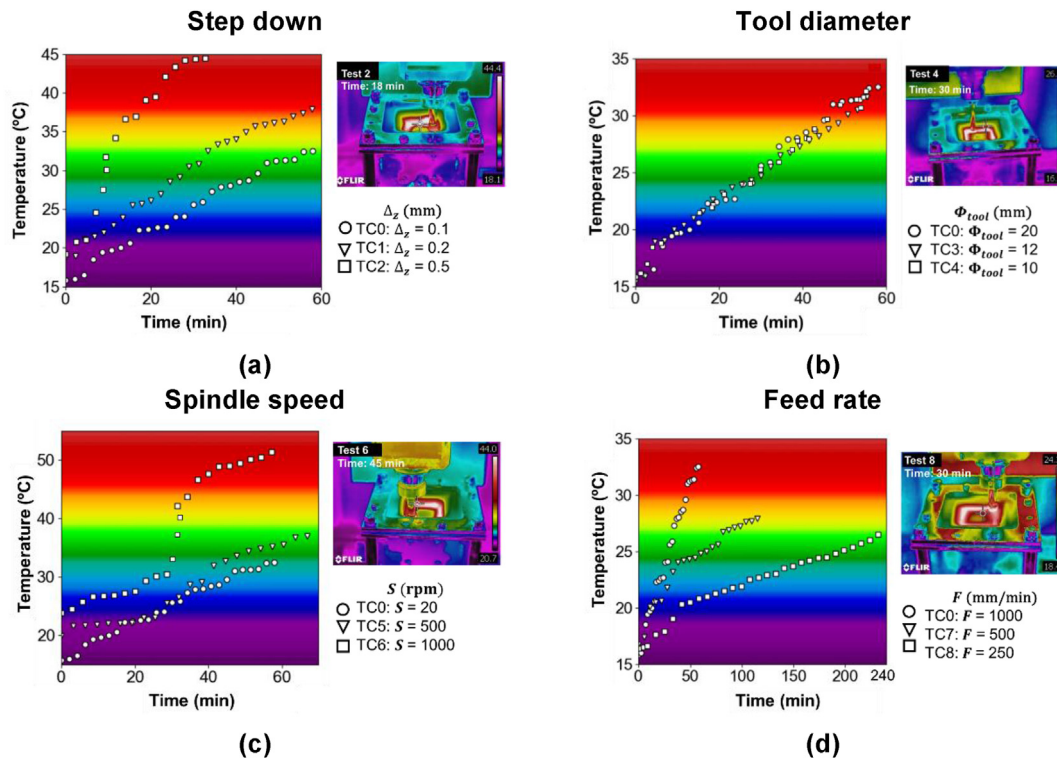
According to the EDS results of the SPIF tests, all of them contained carbon and hydrogen typical of the organic chemistry of the material. In addition, all the tests showed higher or

lower quantities of chlorine due to the lubricant used (mineral oil Houghton™ TDN-81) during the tests. In this sense, those fracture surfaces that were in direct contact with the tool and the lubricant had a higher amount of chlorine. On the other hand, those surfaces that were on the outside face of the pyramid (twisting surface), had less amount of chlorine as they had no direct contact with the lubricant. The extracted EDS also served to confirm that there were no other inclusions on the specimens that could come from dust or dirt.

To sum up, Table 4 presents a comparative analysis of the three modes of failure attained, i.e. fracture, twisting, and crazing. To this respect, the test TC0 is used as a reference for carrying out the comparison with the other SPIF tests. Table 4

**Table 4 – Comparative analysis of the failure modes indicating the main microstructural similarities and differences between the various SPIF tests.**

Macroscopic view of failure	SEM failure and microstructural topologies	SPIF SEM observations
<p>Fracture</p> 	 <ul style="list-style-type: none"> <li>- Irregular surface</li> <li>- Orbed shapes</li> <li>- Spherical shapes</li> </ul>	<ul style="list-style-type: none"> <li>↑ <math>\Delta_z</math> ↑ Stretched fibrils structures</li> <li>↓ <math>\Phi_t</math> ↑ Size of granular shapes</li> <li>↑ S ↑ Crazes holes</li> <li>↓ Size of granular shapes</li> <li>↓ F ↑ Degraded granular shapes</li> </ul>
<p>Twisting</p> 	 <ul style="list-style-type: none"> <li>- Uniform surface</li> <li>- Smooth Zones</li> <li>- Oval shapes</li> </ul>	<ul style="list-style-type: none"> <li>↑ <math>\Delta_z</math> ↑ Smoothness</li> <li>↓ Size of granular shapes</li> <li>↓ <math>\Phi_t</math> ↑↑ Smoothness</li> <li>↑ Uniformity</li> <li>↑ S ↑ Crazes</li> <li>↓ Uniformity</li> <li>↑ Presence of holes</li> <li>↓ F ↑ Crazes</li> <li>↓ Uniformity</li> </ul>
<p>Crazing</p> 		<p>Crazing appears when ↑ S</p> <ul style="list-style-type: none"> <li>- Cracks</li> <li>- Nucleation of voids</li> <li>- Cavities spread</li> <li>- Fibrils</li> <li>- Cavitation hole</li> </ul>



**Fig. 12 – Evolution of temperature versus time of each test varying with respect to reference test TC0: (a) step down, (b) tool diameter, (c) spindle speed and (d) feed rate.**

shows the macroscopic view (of TC0) corresponding to the failure mode as well as the SEM image (In the TC0 specimen  $\times 850$  magnification) together with the main morphological features observed on the surface. In addition, Table 4 shows a series of observations extracted from the other SEM tests assuming the following notation for variation with respect to TC0:  $\uparrow \Delta_z$  (increasing the step down, TC2),  $\downarrow \phi_t$  (decreasing the tool diameter, TC4),  $\uparrow S$  (increasing the spindle speed, TC6) and,  $\downarrow F$  (decreasing the feed rate, TC8).

Concerning failure by fracture, Table 4 allows discussing a number of similarities and differences between the SPIF tests carried out. The ductile fracture surfaces showed a large amount of deformation in the areas analysed. In addition, some zones with irregular surfaces were found, formed by orbs and spherical shapes. The results of the SEM tests in SPIF allowed noticing that this surface could change depending on the test conditions. In global terms, when the step down was increased, shapes more elongated than spherical appeared. In the same regard, decreasing the tool diameter resulted in higher spherical shapes, whereas as the spindle speed increased, certain areas affected by crazing were noticed showing the formation of small holes. Furthermore, the size of the granular shapes decreased compared to the reference test. Finally, it must be also pointed out that decreasing the feed rate allowed observing a surface apparently more degraded than in the other cases, possibly due to the extended duration of the test.

In the case of the failure mode by twisting in Table 4, the SEM analysis of the twisting surfaces revealed much greater uniformity than in the case of the fracture surfaces. Indeed, twisting

zones presented smoother surfaces although they contained certain oval shapes. The SEM results showed that an increase in step down resulted in an even more uniform surface as well as a decrease in the size of the granular shapes. On the other hand, a decrease in the tool size showed the smoothest surface of all the tests performed, as well as a clear uniformity with nearly no spherical shapes. In addition, the increase in the spindle speed resulted in the appearance of crazing over the twisting surface, showing a number of cavities propagating as cracks. Finally, a decrease of the feed rate indicated a reduction in the uniformity of the sample, as well as certain areas with crazing due to the spread of cracking on the sample.

Finally, the third failure mode analysed in Table 4 was the appearance of crazing during the SPIF process in the test TC6. This brittle failure mode was also observed by means of the SEM analysis, starting the cavitation process with the formation of the craze that spreads and ends up breaking, giving rise to the crack. Crazing is favoured by several conditions such as high strain rates, cyclic loadings, exposure to external agents, among others [36]. The following section (section 3.3) further discusses the effect of temperature that increased as a consequence of a higher spindle speed, which may have led to the occurrence of crazing. In addition, the authors are currently working on an investigation that studies more intensively crazing and other failure modes using SEM analysis.

### 3.3. Temperature analysis

The temperature data during the SPIF tests were captured using a thermographic camera FLIR™ model T430sc. To this

regard, Fig. 12 depicts the evolution of the maximum temperature along each experiment. The tests are grouped by target process parameter as follows: Fig. 12a analysing the variations of step down (TC0, TC1, TC2), Fig. 12b the variation of tool diameter (TC0, TC3, TC4), Fig. 12c the variation of spindle speed (TC0, TC5 and TC6), and finally Fig. 12d, the variation of feed rate (TC0, TC7 and TC8). This temperature analysis (temperature versus time) is provided along with the contour caption of the sample temperature distribution for the tests TC2, TC4, TC6 and TC8, respectively, by the end of each experiment. As can be seen, depending on each test conditions, the final time can be sensibly different, especially for the cases of variations concerning step down and feed rate.

Firstly, Fig. 12a shows the temporal evolutions of the temperature obtained for the variation of the step down compared to the reference test. The temperature data of TC0 (step down 0.1 mm) is represented with circles, for TC1 (step down 0.2 mm) with inverted triangles and for TC2 (step down 0.5 mm) with squares. TC1 showed higher values of temperature compared to TC0, although their temperature trajectories had a similar trend. It must be noticed that, in the case of TC2, the duration of the experiment was quite shorter than the rest of the tests (about 35 min) due to the higher step down resulting in a quicker reaching of the failure depth. In this sense, higher values of step downs also give rise to a greater tool-sheet contact area and consequently, an increase in the total frictional energy that is dissipated as heat. These results are in concordance with the previous work by Bagudanch et al. [37], which found an increase in the temperature level and in the process time for higher values of the step down in SPIF of UHMWPE sheet. In a recent work by Yang et al. [38], a series of hot forming SPIF experiments in PEEK sheet were performed using pyramid frustum geometries both with a constant wall angle and varying the wall angle. In that work, the level of maximum forming temperature did also increase with the increase of the step down selected for the SPIF test.

Secondly, Fig. 12b presents the resulting temperatures of changing the tool diameter with respect to TC0 in the SPIF tests. The temperature evolution for TC0 (tool diameter

a	b	c	T <sub>0</sub> (°C)	R <sup>2</sup>
34.81 ± 6.793	1.561 ± 0.228	0.018 ± 0.004	19	0.9138

20 mm) is again represented with circles, for TC3 with inverted triangles (tool diameter 12 mm) and for TC4 (tool diameter 10 mm) with squares. In this case, the tool diameters for TC3 and TC4 were very similar, and consequently they did not show a significant change in the evolution of testing temperature. The comparison between TC0 (tool diameter 20 mm) and TC4 (tool diameter 10 mm) did not either show a significant variation in temperature, presenting though TC0 a slightly higher level of temperature than TC4. This fact may be related to friction, as far as higher tool diameters produce a larger contact area between the tool and the sheet, making it more difficult to dissipate the heat generated as a result of this friction. According to Bagudanch et al. [37], the UHMWPE sheet presented an increase of temperature rise with the tool diameter. To this regard, Hussain et al. [30] studied the effect of temperature variations on the ductility of PVC and PE. This work used the parameter  $\Delta T/m_p$  (where  $\Delta T$  is the rise in temperature and  $m_p$  is the melting point of the polymer) as an index to indicate the softening caused by processing heat. The formability increased with the parameter  $\Delta T/m_p$  depending on the polymeric material, i.e. for PVC formability increased with it, but in the case of PE, formability was contrarily reduced [30].

Thirdly, Fig. 12c shows the evolutions of temperature obtained for the variation of the spindle speed compared to the reference test. In this case, the temperature evolution for TC5 was represented with inverted triangles (spindle speed 500 rpm) and for TC2 (spindle speed 1000 rpm) with squares. The evolutions of temperature for TC0 and TC5 were similar, although TC5 reached a higher level of temperature. On the other hand, TC6 showed an intense change in temperature, presenting a large change in the slope of the path for about

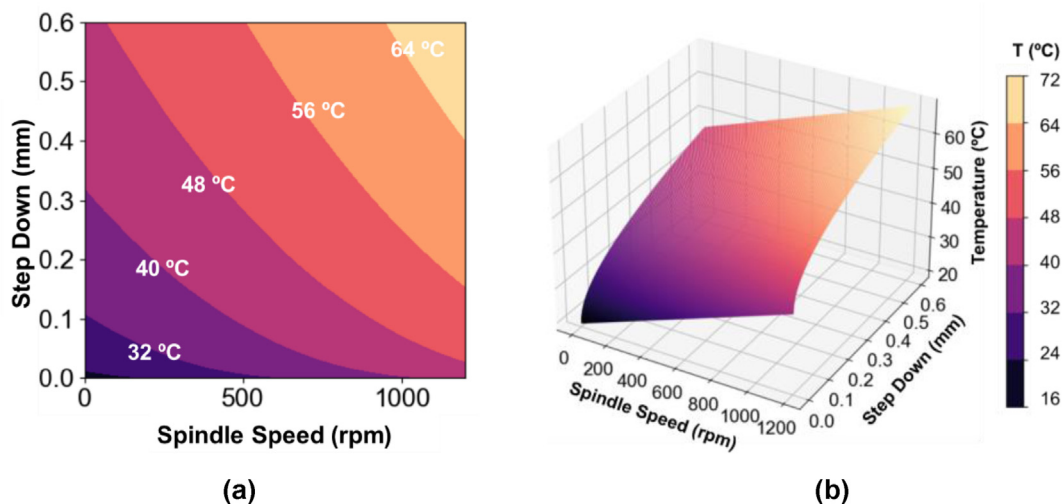
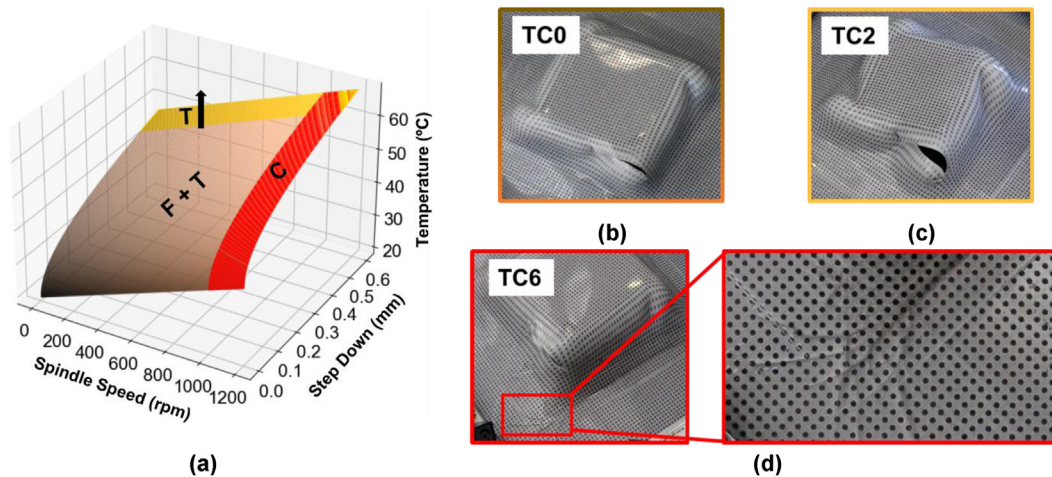


Fig. 13 – The plot of the equation for maximum temperature ( $T_{max}$ ) as a function of the step down ( $\Delta_z$ ) and the spindle speed ( $S$ ) through (a) the 2D contour (b) the 3D logarithmic surface.





**Fig. 14 – (a) Graphical representation of the maximum temperature ( $T_{max}$ ) provided by the regression as a function of the step down ( $\Delta_z$ ) and the spindle speed ( $S$ ) presenting the three obtained modes of failure, also depicting the failure zone for (b) TC0 with failure by twisting and fracture, (c) TC2 showing increased twisting, and (d) TC6 presenting failure by crazing.**

minute 30. Indeed, as a result of the higher spindle speed of TC6 (1000 rpm), the forming temperature increased sensibly. This effect may be also related with the degradation of material resulting in crazing. In this sense, Bagudanch et al. [37] identified the spindle speed as the key parameter affecting the process temperature, being a remarkable rise of heat generated due to tool-sheet friction produced for different polymer materials. Specifically, the case of UHMWPE experimented a variation of 35–40 °C considering the a variation of the spindle from free to 2000 rpm [37].

Finally, Fig. 12d presents the evolutions of temperatures due to the change of the feed rate. The temperature data for TC0 (1000 mm/min) is once again represented with circles, for TC7 (feed rate 500 mm/min) with inverted triangles and for TC8 (feed rate 250 mm/min) with squares. Comparing the three evolutions, it must be concluded that the decrease in the feed rate results in the decrease of the level of temperature attained. The lowest level of temperature was for the test TC8, being for this case the SPIF test duration about 4 h (maximum duration achieved of all the tests performed). For TC8, the forming temperature maintained relatively stable during the test compared to TC0 and TC7, probably as a result of the combination of low feed rate and lubrication. The same results were shown in previous research works [12,27], being a decrease in temperature produced by a decrease in the values of the feed rate.

In conclusion, after analysing the results of the maximum temperature achieved, the two most important parameters were the step down and the spindle speed. Taking this into consideration, an empirical model to predict the maximum temperature attained was developed. To this regard, Eq. (2) is able to provide a fair prediction of the maximum temperature ( $T_{max}$ ) as a function of these process parameters, i.e. the step down and the spindle speed ( $\Delta_z$ ,  $S$ ), as a result of a multivariate logarithmic regression.

$$T_{max}(\Delta_z, S) = a * b^{\log(\Delta_z)} + c * S + T_0 \quad (2)$$

The initial temperature ( $T_0$ ) of the experiments was the room temperature, on average 19 °C. Python SciPy [39] and Python NumPy [40] libraries were used in order to assess the terms of the multivariate logarithmic regression, which summarised in Table 5.

Thus, the values provided in Table 5 are used in Eq. (2) for providing a numerical expression of the maximum temperature ( $T_{max}$ ) as a function of these process parameters.

To this regard, Fig. 13 presents different contour plots of Eq. (3) using the Python Matplotlib library [41]. As can be seen in Fig. 13a, the empirical model showed that higher spindle speeds and higher step downs produced higher levels of maximum temperature. On the other hand, Fig. 13b depicts the surface multivariable function, showing the characteristic shape of the surface representing a logarithmic function. As expected, the combination of high step down (0.6 mm) and high spindle speed (1000 rpm) results in a high level of temperature. As a result, an undesirable failure mode such as crazing may occur under these conditions. Intermediate values of step down (around 0.3) and spindle speed (500 rpm) would results in values of the maximum temperature in the range of 40–48°, which may lead to an increase in formability without resulting in the undesirable appearance of failure by crazing. In a recent study by Wu et al. [42], the impact of various thermo-mechanical treatments on the brittle-to-ductile transition in a slightly ductile polycarbonate during uniaxial stretching is examined. The researchers use photoelasticity to analyse stress distribution in fractured and high-temperature pre-stretched samples. The investigation concludes that the brittle-to-ductile transition is associated with microstructure changes, which can be detected through photoelasticity. Significant shape and microstructure alterations necessitate high-temperature pre-deformation, leading to anisotropic material properties and fracture toughness. The transition is dependent on loading modes during pre-deformation and subsequent fracture loading, with pre-deformation magnitude, temperature, and

the original material's maximum deformation capability being crucial factors influencing the transition's significance.

To sum up, Fig. 14 depicts the surface multivariable function together with the likely modes of failure as a result of the corresponding set of process parameters (i.e. step down and spindle speed). Although all the tests carried out presented the combination of fracture and twisting for a certain final depth, it must be taken into account that the higher step down, the faster incipient twisting in the specimen. Indeed, for step downs higher than 0.5 mm, the twisting effect would be more severe on the specimen, which is represented with a T together with an arrow in the yellow zone in Fig. 14a. On the other hand, as observed in the experiments for a spindle speed of 1000 rpm, higher levels of spindle speed may lead to the appearance of crazing. As a consequence, the higher spindle speed, the more probable that the specimen presents crazing, as depicted with a C within the red zone in Fig. 14a. In addition, the 3 modes of failure are also represented in Fig. 14b for the test TC0, TC2 and TC6.

#### 4. Conclusions

This research study presents a critical experimental investigation of PC sheets deformed by SPIF, providing an overall analysis of the influence of the main process parameters on formability and their connection with the different modes of failure attained. In order to establish a complete framework for the selected material, both an evaluation of the micro-mechanism of failure and the evolutions of temperature for the different test conditions considered were performed. The study was carried out in terms of principal strains evaluated within the material forming limit diagrams obtained independently.

The experimental results evidenced the forming limits of the PC sheet material as well as the failure mechanisms in SPIF for a wide range of testing conditions. The SPIF tests with the selected frusto-pyramidal geometry gave rise to three different modes of failure: twisting, fracture and crazing. The analysis of temperature carried out allowed establishing the main differences in the evolutions of forming temperature depending on the selected set of process parameters. The whole failure surfaces were also analysed by using different SEM magnifications and the main phenomenological differences between the different tests were shown and critically discussed.

Beyond the general conclusions established above, a number of findings and particular conclusions were achieved in this study, and they are presented in what follows.

- Concerning the characterization of PC sheet, the overall procedures established in recent research works by the authors allowed adapting and applying these methodologies, providing general procedures for the evaluation of the necking and fracture for polymer sheets.
- Most of the typical forming conditions in SPIF led to failure by fracture in the nonappearance of necking due to crack opening along the circumferential direction in mode I of fracture mechanics.

- Regarding the specific geometry of the pyramidal frustum used for the SPIF tests: (i) all the tests presented twisting combined with fracture, (ii) twisting increased with the step down and, (iii) higher values of spindle speed promoted crazing.
- In terms of spifability, the sections analysed in the zone of the pyramidal wall (close to plane strain conditions) showed that high values of the step down and the spindle speed allowed reaching high levels of strains. On the contrary, the sections analysed in the zone of the pyramid corner (biaxial conditions) did not present a significant difference in terms of the maximum strains reached.
- The micro-mechanism of failure analysed allowed establishing the following main difference between the surfaces studied: (i) most of the fracture surfaces were formed by spherical shapes having the lowest possible energy under stress, (ii) the surface at twisting seemed to be more uniform and (iii) the crazing zone presented small cracks due to the cavitation process.
- The failure surfaces analysed using SEM allowed observing surfaces with high deformation (ductile failure) and surfaces with low deformation (brittle failure). The fracture surfaces analysed had in general striated and/or spherical shapes depending on the conditions, whereas the twisting surfaces showed great uniformity and smoothness. In the case of crazing, micro voids and cracks typical of brittle fracture were observed.
- Concerning the thermal analysis, the most relevant parameters resulting in higher temperatures were the step down and the spindle speed. Both parameters produced a notably increase in the evolution of the forming temperature. The proposed empirical model related those parameters with the maximum temperature by means of a logarithmic function, resulting in the increase of the step down and the spindle speed in an increase of temperature. Finally, a failure surface depicting the maximum temperature together with the likely modes was established and graphically depicted.

#### Declaration of Competing Interest

The authors declare that they have no known competing financial interests or personal relationships that could have appeared to influence the work reported in this paper.

#### Acknowledgments

The authors would like to express their gratitude to the Major Grant TED2021-131153B-C22 funded by MCIN/AEI/10.13039/501100011033 and the European Union through the Program NextGenerationEU/PRTR. This is the main project funding this research work and paying for the entire APC fee.

In addition, the authors would also like to acknowledge previous funding received from the Regional Government of Andalusia under the Grant with reference P18-RT-3866 funded

under the framework US/JUNTA/FEDER UE of the “PAIDI 2020: Proyectos I+D+I” and the Fundação para a Ciência e da Tecnologia of Portugal, through IDMEC, under LAETA, project UIDB/50022/2020.

## REFERENCES

- [1] Legrand DG, Bendler JT. Handbook of polycarbonate science and technology. 1st ed. New York: CRC Press (Marcel Dekker Inc); 1999. <https://doi.org/10.1201/9781482273694>.
- [2] The industrial revolution of the 21st century Popkova EG, Ragulina YV, Bogoviz AV, editors. Ind. 4.0 Ind. Revolut. 21st Century. 2006;169:249. <https://doi.org/10.1007/978-3-319-94310-7>.
- [3] Xu X, Lu Y, Vogel-Heuser B, Wang L. Industry 4.0 and industry 5.0: inception, conception and perception. J Manuf Syst 2021;61:530–5. <https://doi.org/10.1016/j.jmsy.2021.10.006>.
- [4] Duc-Toan N, Seung-Han Y, Dong-Won J, Tae-Hoon C, Young-Suk K. Incremental sheet metal forming: numerical simulation and rapid prototyping process to make an automobile white-body. Steel Res Int 2011;82:795–805. <https://doi.org/10.1002/SRIN.201000284>.
- [5] Hussain G, Khan HR, Gao L, Hayat N. Guidelines for tool-size selection for single-point incremental forming of an aerospace alloy. Mater Manuf Process 2013;28:324–9. <https://doi.org/10.1080/10426914.2012.700151>.
- [6] Cheng Z, Li Y, Xu C, Liu Y, Ghafoor S, Li F. Incremental sheet forming towards biomedical implants: a review. J Mater Res Technol 2020;9:7225–51. <https://doi.org/10.1016/J.JMRT.2020.04.096>.
- [7] Chen LF, Chen F, Gatea S, Ou H. PEEK based cranial reconstruction using thermal assisted incremental sheet forming. <https://doi.org/10.1177/09544054211045904>; 2021.
- [8] Franzen V, Kwiatkowski L, Martins PAF, Tekkaya AE. Single point incremental forming of PVC. J Mater Process Technol 2009;209:462–9. <https://doi.org/10.1016/j.jmatprotec.2008.02.013>.
- [9] Martins PAF, Kwiatkowski L, Franzen V, Tekkaya AE, Kleiner M. Single point incremental forming of polymers. CIRP Ann - Manuf Technol 2009;58:229–32. <https://doi.org/10.1016/j.cirp.2009.03.095>.
- [10] Silva MB, Alves LM, Martins PAF. Single point incremental forming of PVC: experimental findings and theoretical interpretation. Eur J Mech Solid 2010;29:557–66. <https://doi.org/10.1016/j.euromechsol.2010.03.008>.
- [11] Davarpanah MA, Mirkouei A, Yu X, Malhotra R, Pilla S. Effects of incremental depth and tool rotation on failure modes and microstructural properties in Single Point Incremental Forming of polymers. J Mater Process Technol 2015;222:287–300. <https://doi.org/10.1016/j.jmatprotec.2015.03.014>.
- [12] Le VS, Ghiotti A, Lucchetta G. Preliminary studies on single point incremental forming for thermoplastic materials. Int J Material Form 2008;1:1179–82. <https://doi.org/10.1007/s12289-008-0191-0>.
- [13] Bagudanch I, Garcia-Romeu ML, Sabater M. Incremental forming of polymers: process parameters selection from the perspective of electric energy consumption and cost. J Clean Prod 2016;112:1013–24. <https://doi.org/10.1016/j.jclepro.2015.08.087>.
- [14] Durante M, Formisano A, Lambiase F. Incremental forming of polycarbonate sheets. J Mater Process Technol 2018;253:57–63. <https://doi.org/10.1016/j.jmatprotec.2017.11.005>.
- [15] Yang Z, Chen F. Mechanism of twist in incremental sheet forming of thermoplastic polymer. Mater Des 2020;195:108997. <https://doi.org/10.1016/J.MATDES.2020.108997>.
- [16] Rosa-Sainz A, Centeno G, Silva MB, Vallellano C. Experimental failure analysis in polycarbonate sheet deformed by spif. J Manuf Process 2021;64:1153–68. <https://doi.org/10.1016/j.jmapro.2021.01.047>.
- [17] Martínez-Donaire AJ, García-Lomas FJ, Vallellano C. New approaches to detect the onset of localised necking in sheets under through-thickness strain gradients. Mater Des 2014;57:135–45. <https://doi.org/10.1016/j.matdes.2014.01.012>.
- [18] Centeno G, Bagudanch I, Martínez-Donaire AJ, García-Romeu ML, Vallellano C. Critical analysis of necking and fracture limit strains and forming forces in single-point incremental forming. Mater Des 2014;63:20–9. <https://doi.org/10.1016/j.matdes.2014.05.066>.
- [19] Rosa-Sainz A, Centeno G, Silva MB, López-Fernández JA, Martínez-Donaire A, Vallellano C. On the determination of forming limits in polycarbonate sheets. Materials 2020;13:1–17. <https://doi.org/10.3390/ma13040928>.
- [20] ASTM-D638-14. Standard test method for tensile properties of plastics. ASTM Stand.; 2014.
- [21] ISO12004-2. Metallic materials-Sheet and strip-Determination of forming limit curves Part 2: determination of forming limit curves in laboratory. 2008.
- [22] Centeno G, Martínez-Donaire AJ, Morales-Palma D, Vallellano C, Silva MB, Martins PAF. Novel experimental techniques for the determination of the forming limits at necking and fracture. Mater. Form. Mach. Res. Dev. 2015:1–24. <https://doi.org/10.1016/B978-0-85709-483-4.00001-6>.
- [23] GOM optical measuring techniques, ‘ARGUS v5.4 user manual’. GOM mbH; 2005. [www.gom.com](http://www.gom.com).
- [24] Schenk T. Introduction to photogrammetry. Dep. Civ. Environ. Eng. Geod. Sci. 2005:79–95. Ohio State Univ. [http://gscphoto.ceegs.ohio-state.edu/courses/GeodSci410/docs/GS410\\_02.pdf](http://gscphoto.ceegs.ohio-state.edu/courses/GeodSci410/docs/GS410_02.pdf). [Accessed 28 June 2021].
- [25] Marques TA, Silva MB, Martins PAF. On the potential of single point incremental forming of sheet polymer parts. Int J Adv Manuf Technol 2012;60:75–86. <https://doi.org/10.1007/s00170-011-3585-y>.
- [26] Formisano A, Boccarusso L, Carrino L, Lambiase F, Minutolo FMC. Single point incremental forming: formability of PC sheets. AIP Publishing LLC AIP Publishing; 2018. p. 100006. <https://doi.org/10.1063/1.5034946>. AIP Conf. Proc.
- [27] Bagudanch I, Garcia-Romeu ML, Centeno G, Elías-Zúñiga A, Ciurana J. Forming force and temperature effects on single point incremental forming of polyvinylchloride. J Mater Process Technol 2015;219:221–9. <https://doi.org/10.1016/j.jmatprotec.2014.12.004>.
- [28] Bagudanch I, Centeno G, Vallellano C, Garcia-Romeu ML. Revisiting formability and failure of polymeric sheets deformed by Single Point Incremental Forming. Polym Degrad Stabil 2017;144:366–77. <https://doi.org/10.1016/j.polymdegradstab.2017.08.021>.
- [29] Conte R, Gagliardi F, Ambrogio G, Filice F, Russo P. Performance analysis of the incremental sheet forming on PMMA using a combined chemical and mechanical approach. AIP Conf Proc 2017;1896:080026. <https://doi.org/10.1063/1.5008106>.
- [30] Hussain G, Mahna A, Iqbal A. Response surface analysis of cold formability of polymers in Incremental Sheet Forming: effect of parameters and associated thermal softening. Int J Precis Eng Manuf 2016;17:613–21. <https://doi.org/10.1007/S12541-016-0074-0>.
- [31] Argon AS. The physics of deformation and fracture of polymers. United Kingdom: Cambridge University Press; 2010. <https://doi.org/10.1017/CBO9781139033046>.

- [32] Hayes MD, Edwards DB, Shah AR. Fractography in failure analysis of polymers. United States: Elsevier Inc.; 2015. <https://doi.org/10.1016/c2013-0-01392-8>.
- [33] Zimmerman DL, Jones RW. SEM analysis of polymeric mechanical failures in polyetherimide. *Int. J. Polym. Mater. Polym. Biomater.* 2006;23:151–65. <https://doi.org/10.1080/00914039408029327>.
- [34] Jansen JA. Fractographic characterization of polycarbonate failure modes. *Annu. Tech. Conf. - ANTEC, Conf. Proc.* 2004;3:4094–9.
- [35] Wei H, Hussain G, Heidarshenas B, Alkahtani M. Post-forming mechanical properties of a polymer sheet processed by incremental sheet forming: insights into effects of plastic strain, and orientation and size of specimen. *Polymers* 2020;12. <https://doi.org/10.3390/POLYM12091870>.
- [36] Van Krevelen DW, Te Nijenhuis K. Product properties (I). *Prop. Polym.* 2009;819–45. <https://doi.org/10.1016/b978-0-08-054819-7.00025-x>.
- [37] Bagudanch I, Vives-Mestres M, Sabater M, Garcia-Romeu ML. Polymer incremental sheet forming process: temperature analysis using response surface methodology. *Mater Manuf Process* 2017;32:44–53. <https://doi.org/10.1080/10426914.2016.1176191>.
- [38] Yang Z, Chen F, Gatea S, Ou H. Design of the novel hot incremental sheet forming experimental setup, characterization of formability behavior of polyether-etherketone (PEEK). *Int J Adv Manuf Technol* 2020;106:5365–81. <https://doi.org/10.1007/s00170-020-05035-0>.
- [39] Python SciPy. `scipy.optimize.curve_fit` Documentation. [https://docs.scipy.org/doc/scipy/reference/generated/scipy.optimize.curve\\_fit.html](https://docs.scipy.org/doc/scipy/reference/generated/scipy.optimize.curve_fit.html). [Accessed 19 December 2022].
- [40] NumPy Library, Python. <https://numpy.org/doc/stable/>. [Accessed 22 December 2022].
- [41] Matplotlib Python v3.4.2. <https://matplotlib.org/>. [Accessed 25 June 2021].
- [42] Wu X, Wang C, Pek JX, Huang WM. Brittle-to-ductile transition in high temperature pre-stretched polycarbonate. *J Polym Res* 2022;29:1–7. <https://doi.org/10.1007/s10965-022-03282-1>.